Supporting Information

Direct ink writing of high-performance Bi_2Te_3-based thermoelectric materials by quasi-inorganic inks and interface engineering

Zhengshang Wang[a], *Wen Cui*[a], *Hao Yuan*[b], *Xiaoli Kang*[b], *Zhou Zheng*[b], *Longqin Chen*[c], *Qiujun Hu*[d], *Wenbin Qiu*[c], *Jun Tang*[c], *Xudong Cui*[b,*]

[a] Sichuan Research Center of New Materials, 596 Yinhe Road, Shuangliu, Chengdu 610200, PR China

[b] Institute of Chemical Materials, China Academy of Engineering Physics, Mianyang 621900, PR China

[c] Key Laboratory of Radiation Physics and Technology of Ministry of Education, Institute of Nuclear Science and Technology, Sichuan University, Chengdu 610064, China

[d] College of Physics, Sichuan University, Chengdu 610065, China

* Corresponding authors.

E-mail addresses: xudcui@caep.cn

In order to gain more insights into the thermal properties of the as-printed samples, we calculated the thermal conductivity according to the relationship:

$$\kappa_{tot} = \kappa_{ele} + \kappa_{lat} + \kappa_b \qquad \text{¥* MERGEFORMAT (1)}$$

where κ_{tot} is the total thermal conductivities, κ_{lat} is the lattice thermal conductivities, κ_b is the bipolar thermal conductivities, κ_{ele} is the electrical thermal conductivities, respectively. Besides, κ_{ele} can be estimated by Wiedemann–Franz law $\kappa_{ele} = L\sigma T$, as shown in Fig. S7a and S7d.

Since lattice vibration dominate the phonon scattering process above Debye temperature, temperature-dependent κ_{lat} can be extrapolated by the following expression [1, 2]:

$$\kappa_{lat} = A + B \cdot T^{-1} \qquad \text{¥* MERGEFORMAT (2)}$$

where A and B are the fitting parameters. We can achieve the fitted values of A and B, according to the experimental results of $\kappa_{lat} + \kappa_b$ and the calculated ones, before $\kappa_{lat} + \kappa_b$ are governed by κ_b. Then, we could extrapolate the values of κ_{lat} at relatively high temperature, based on the above expressions. Finally, κ_b can be obtained through subtracting the calculated κ_{lat} from $\kappa_{lat} + \kappa_b$ (Fig. S7c and S7f).

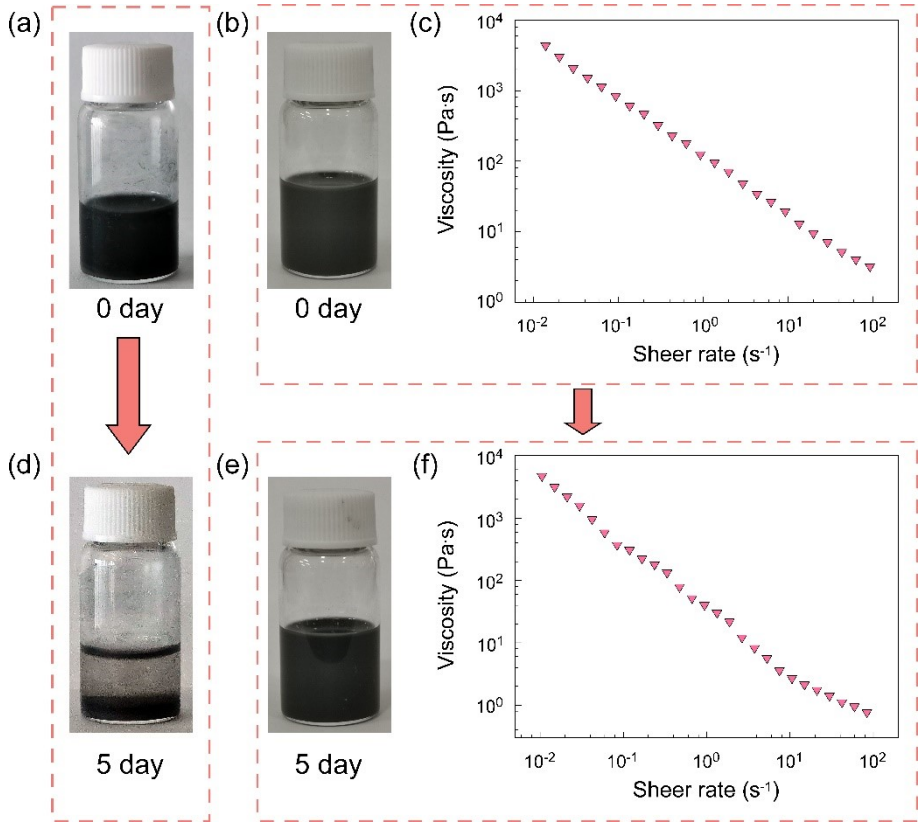

Fig. S1. Stability of Bi_2Te_3-based TE inks. Photographs of inks without (a) and with (b) PAA-PEI binders. (c) Complex viscosity corresponding to TE inks with binders (b). Photographs of inks after 5-days-settlement without (d) and with (e) PAA-PEI binders. (f) Complex viscosity corresponding to TE inks with binders (e).

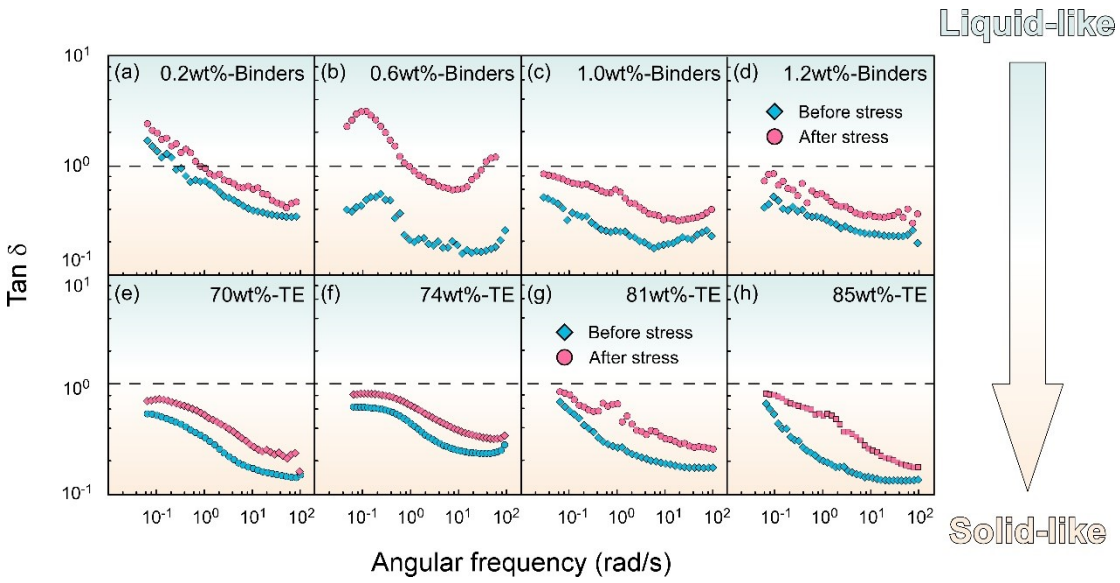

Fig. S2. Loss tangent tanδ curves of TE inks containing 81wt% particles loading with different binders content (a) 0.2wt%, (b) 0.6wt%, (c) 1.0wt%, (d) 1.2wt%. Loss tangent tanδ curves of TE inks containing 1.0wt% binders with various particles loading (e) 70wt%, (f) 74wt%, (g) 81wt%, (h) 85wt%.

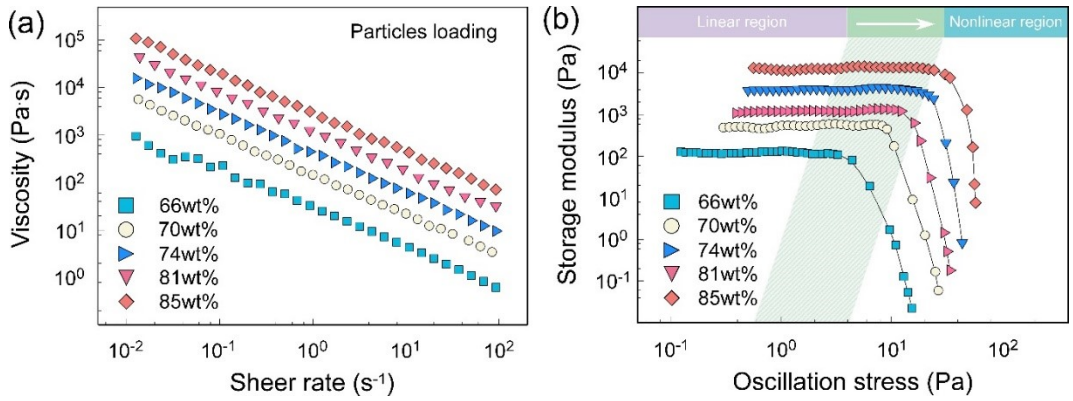

Fig. S3. (a) Complex viscosity and (b) storage modulus curves of 1.0wt% binders TE inks with various particle loadings.

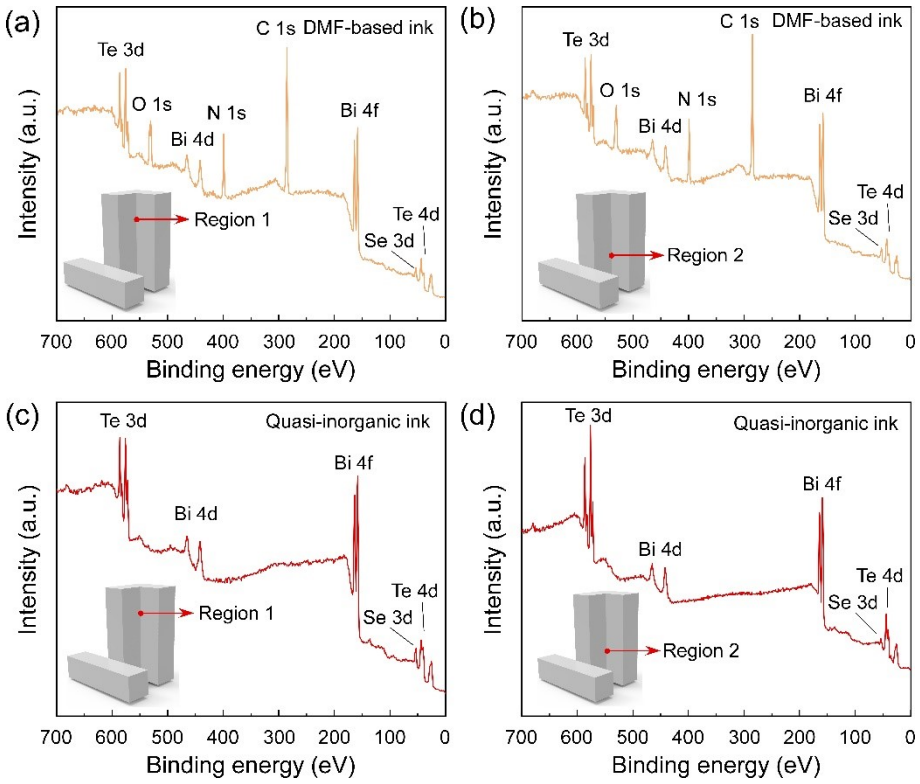

Fig. S4. XPS spectrums of (a) Region 1 and (b) Region 2 selected in *n*-type sample printed by DMF-based inks. XPS spectrums of (c) Region 1 and (d) Region 2 selected in *n*-type sample printed by quai-inorganic inks. The above peaks are indexed to Te 3d, Te 4d, Bi 4d, Bi 4f, Se 3d, C 1s, O 1s, and N 1s, respectively [3, 4].

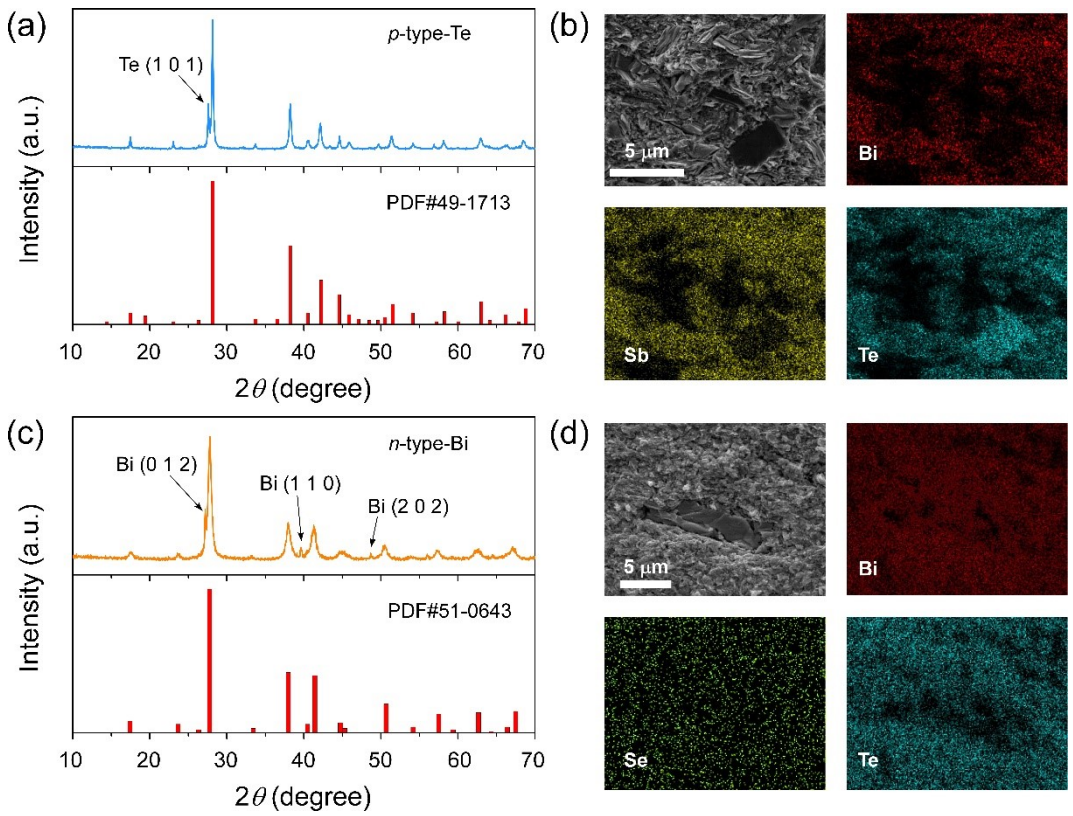

Fig. S5. (a) XRD patterns for 3D-printed *p*-type-Te. (b) Fracture surface morphology and corresponding energy-dispersive spectroscopy (EDS) mapping for 3D-printed *p*-type-Te. (c) XRD patterns for 3D-printed *n*-type-Bi. (d) Fracture surface morphology and corresponding EDS mapping for 3D-printed *n*-type-Bi.

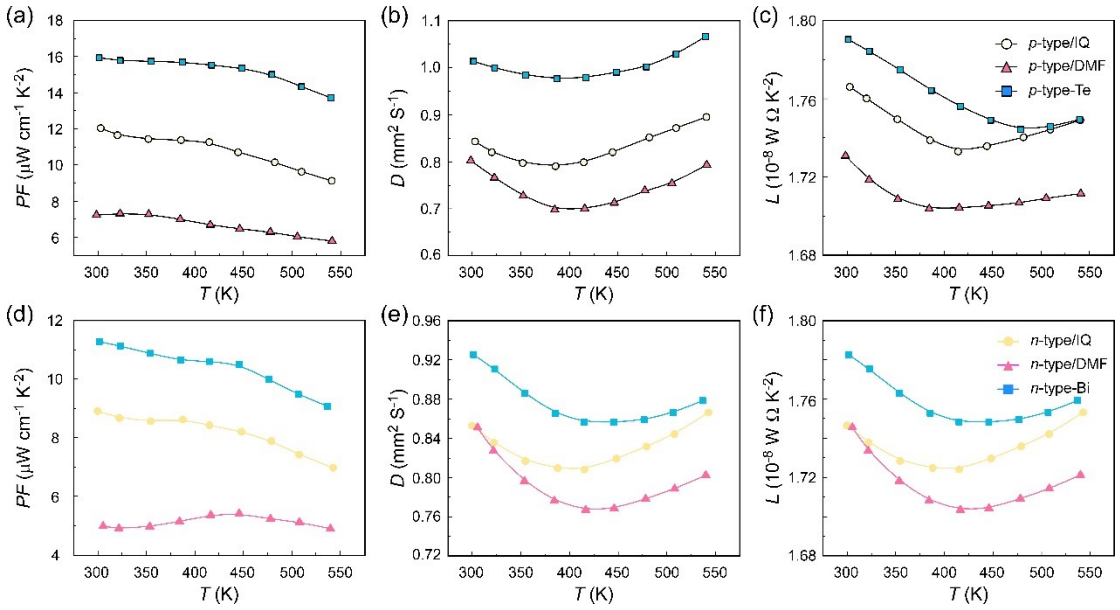

Fig. S6. Temperature-dependent (a) power factor *PF*, (b) thermal diffusivities *D*, (c) Lorenz numbers *L* of 3D-printed *p*-type samples. Temperature-dependent (d) power factor *PF*, (e) thermal diffusivities *D*, (f) Lorenz numbers *L* of 3D-printed *n*-type samples .

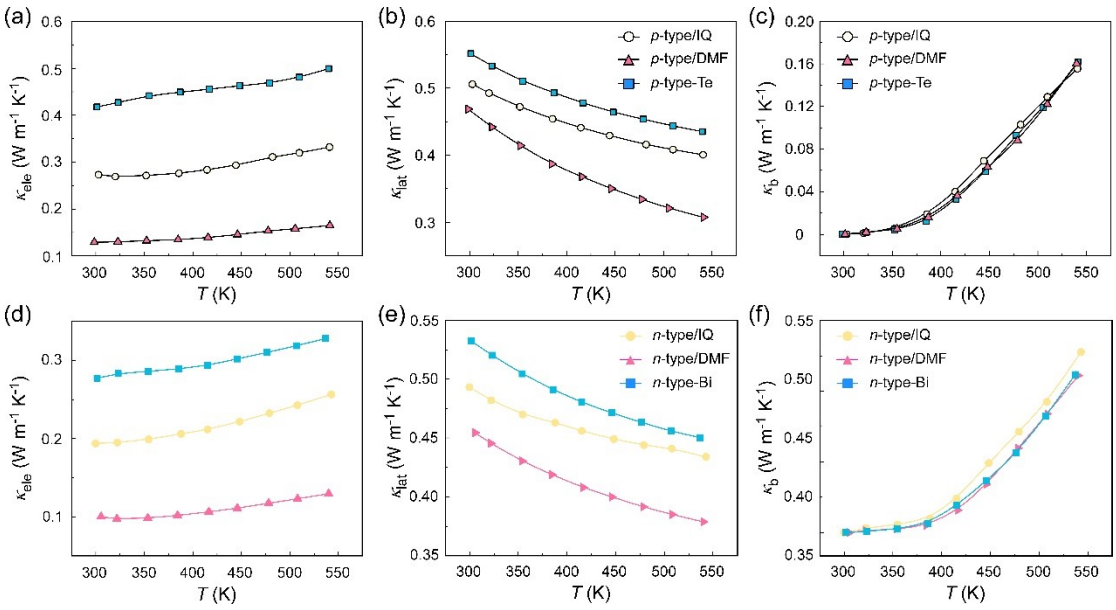

Fig. S7. Temperature-dependent (a) electrical thermal conductivities κ_{ele}, (b) lattice thermal conductivities κ_{lat}, (c) bipolar thermal conductivities κ_{lat} of 3D-printed *p*-type samples. Temperature-dependent (d) electrical thermal conductivities κ_{ele}, (e) lattice thermal conductivities κ_{lat}, (f) bipolar thermal conductivities κ_b of 3D-printed *n*-type samples. The calculation details of bipolar thermal conductivities κ_b had been reported in 3D-printed and bulk Bi_2Te_3-based materials [1].

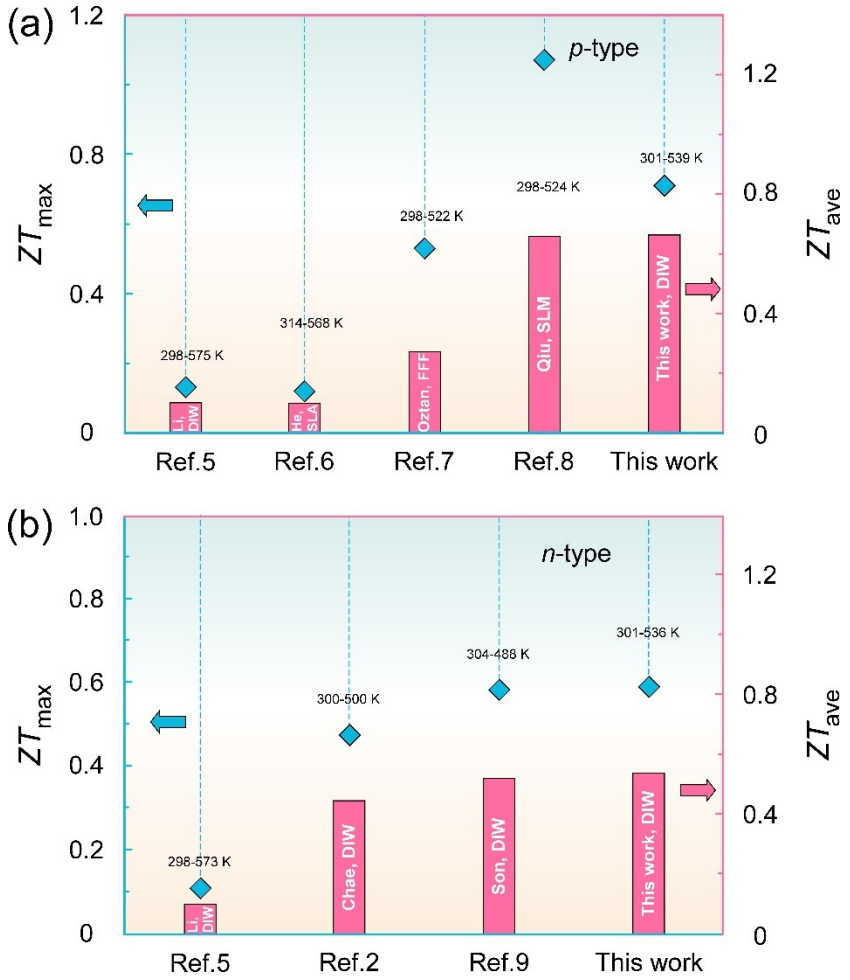

Fig. S8. Comparison of ZT maximum values (ZT_{max}) and average ZT values (ZT_{ave}) with previous reported (a) *p*-type [5-8], and (b) *n*-type [2, 5, 9] 3D-printed Bi_2Te_3-based thermoelectric materials fabricated by DIW, sterolithography apparatus (SLA), fused filament fabrication (FFF), and selective laser melting (SLM).

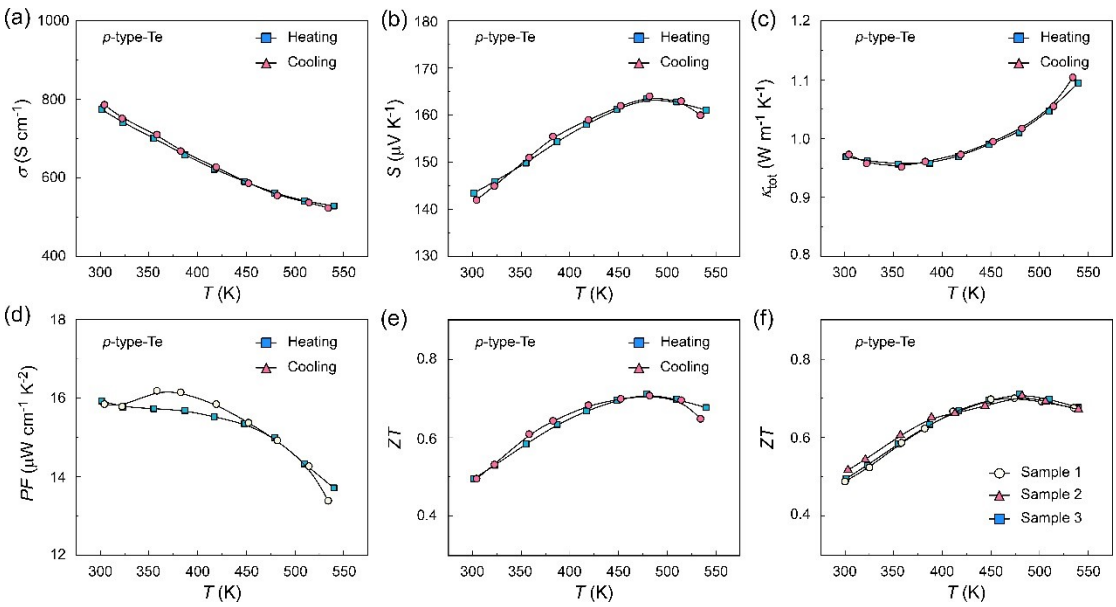

Fig. S9. Stability evaluation of the high-performance 3D-printed *p*-type-Te samples from heating to cooling cycles. (a) Electrical conductivity σ; (b) Seebeck coefficient S; (c) total thermal conductivity κ_{tot}; (d) power factor PF; (e) ZT values; (f) reproducibility of ZT values for three different *p*-type-Te samples printed independently.

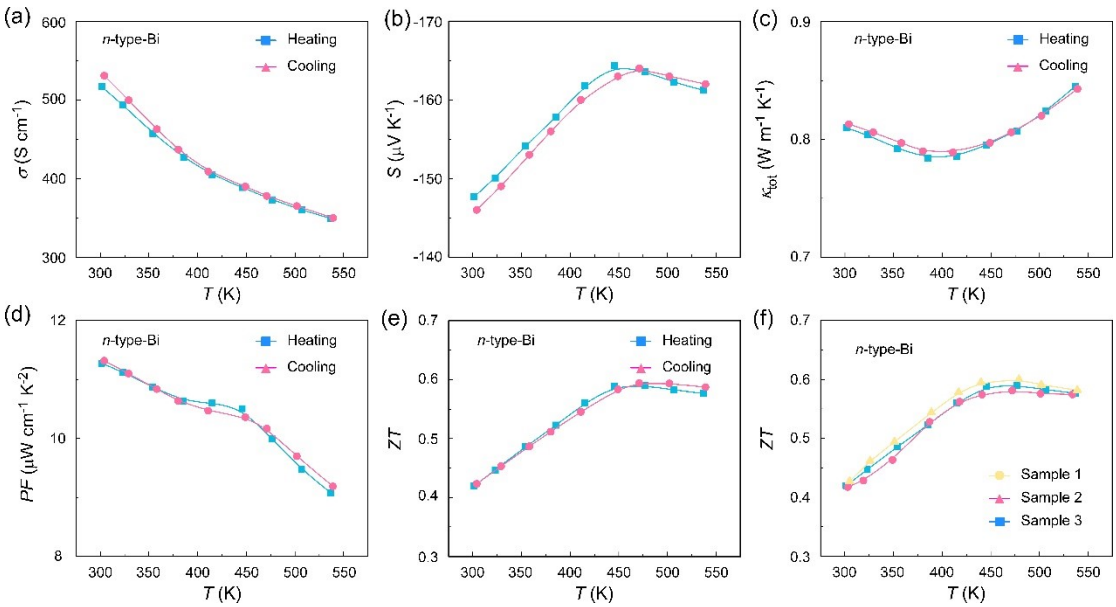

Fig. S10. Stability evaluation of the high-performance 3D-printed *n*-type-Bi samples from heating to cooling cycles. (a) Electrical conductivity σ; (b) Seebeck coefficient S; (c) total thermal conductivity κ_{tot}; (d) power factor PF; (e) ZT values; (f) reproducibility of ZT values for three different *n*-type-Bi samples printed independently.

Table S1. The calculated particle loading of TE inks, density, and relative density of *p*-type/IQ, *n*-type/IQ, *p*-type/DMF, *n*-type/DMF, *p*-type/Te, *n*-type/Bi.

	Particle loading	Density (g/cm3)	Relative density
p-type/IQ	65.5wt%	2.44	35.9%
	70.4wt%	2.86	42.1%
	74.0wt%	3.70	54.4%
	81.1wt%	5.21	76.6%
	85.1wt%	5.42	79.7%
n-type/IQ	65.5wt%	2.36	30.7%
	70.4wt%	2.98	38.7%
	74.0wt%	3.57	46.4%
	81.1wt%	4.92	63.9%
	85.1wt%	5.08	66.1%
p-type/DMF	81.1wt%	4.37	64.2%
n-type/DMF	81.1wt%	4.11	53.4%
p-type/Te	81.1wt%	5.61	82.5%
n-type/Bi	81.1wt%	5.52	71.8%

Table S2. The output performance of the TE devices.

Materials	*p*: segmented BiSbTe	*p*: $Bi_{0.5}Sb_{1.5}Te_3$ *n*: Bi_2Te_3	*p*: $Bi_{0.4}Sb_{1.6}Te_3$ *n*: $Bi_2Sb_{2.7}Se_{0.3}$	*p*: $Bi_{0.5}Sb_{1.5}Te_{3.0}$ *n*: $Bi_{2.0}Te_{2.7}Se_{0.3}$
Device structure	Tri-block	Annular	Half annular	Half annular
Method	DIW	DIW	DIW	DIW
Number of legs	1	5	3	3
ΔT (K)	236.1	54.6	39.2	55.6
V_{OC} (mV)	53	60.8	27	40.61
V_{OC} per leg (mV)	53	12.16	9	13.53
P_{max} (μW)	260	678	1420	380
P_{max} per leg (μW)	260	135.6	473.3	126.6
Reference	[1]	[5]	[9]	This work

References

[1] S. E. Yang, F. Kim, F. Ejaz, G. S. Lee, H. Ju, S. Choo, J. Lee, G. Kim, S.-h. Jung and S. Ahn, Composition-segmented BiSbTe thermoelectric generator fabricated by multimaterial 3D printing, Nano Energy, 81, (2021), 105638.

[2] F. Kim, S. E. Yang, H. Ju, S. Choo, J. Lee, G. Kim, S.-h. Jung, S. Kim, C. Cha, K. T. Kim, S. Ahn, H. G. Chae and J. S. Son, Direct ink writing of three-dimensional thermoelectric microarchitectures, Nature Electronics, 4, (2021), 579-587.

[3] C. R. Thomas, M. K. Vallon, M. G. Frith, H. Sezen, S. K. Kushwaha, R. J. Cava, J. Schwartz and S. L. Bernasek, Surface oxidation of $Bi_2(Te, Se)_3$ topological insulators depends on cleavage accuracy, Chemistry of Materials, 28, (2016), 35-39.

[4] J.-D. Musah, A. Ilyas, A. Novitskii, I. Serhiienko, K. O. Egbo, G. Saianand, V. Khovaylo, S. Kwofie, K. M. Yu and V. A. Roy, Effective decoupling of seebeck coefficient and the electrical conductivity through isovalent substitution of erbium in bismuth selenide thermoelectric material, Journal of Alloys and Compounds, 857, (2021), 157559.

[5] N. Su, P. Zhu, Y. Pan, F. Li and B. Li, 3D-printing of shape-controllable thermoelectric devices with enhanced output performance, Energy, 195, (2020), 116892.

[6] M. He, Y. Zhao, B. Wang, Q. Xi, J. Zhou and Z. Liang, 3D printing fabrication of amorphous thermoelectric materials with ultralow thermal conductivity, Small, 11, (2015), 5889-5894.

[7] C. Oztan, S. Ballikaya, U. Ozgun, R. Karkkainen and E. Celik, Additive manufacturing of thermoelectric materials via fused filament fabrication, Applied Materials Today, 15, (2019), 77-82.

[8] J. Qiu, Y. Yan, T. Luo, K. Tang, L. Yao, J. Zhang, M. Zhang, X. Su, G. Tan and H. Xie, 3D Printing of highly textured bulk thermoelectric materials: mechanically robust BiSbTe alloys with superior performance, Energy & Environmental Science, 12, (2019), 3106-3117.

[9] F. Kim, B. Kwon, Y. Eom, J. E. Lee, S. Park, S. Jo, S. H. Park, B.-S. Kim, H. J. Im and M. H. Lee, 3D printing of shape-conformable thermoelectric materials using all-inorganic Bi_2Te_3-based inks, Nature Energy, 3, (2018), 301.